ELSEVIER

International Journal of Solids and Structures 41 (2004) 1039–1059

INTERNATIONAL JOURNAL OF SOLIDS and STRUCTURES

www.elsevier.com/locate/ijsolstr

Dynamic buckling of periodically stiffened shells: application to supercavitating vehicles

Massimo Ruzzene *

School of Aerospace Engineering, Georgia Institute of Technology, 270 Ferst Drive, Atlanta, GA 30332-0150, USA

Received 1 December 2002; received in revised form 13 July 2003

Abstract

Supercavitating vehicles undergo high longitudinal forces as result of their high underwater velocity. The drag force compresses axially the body and may cause its buckling. In addition, the unsteady characteristics of the system composed of cavity and vehicle generate time-varying longitudinal loads that are sources of parametric resonances. Supercavitating vehicles are here modeled as thin axisymmetric shells acted upon by time-varying axial compressive forces. A finite element model is developed to predict the shells behavior and to perform the buckling analysis. The longitudinal forces are considered to vary periodically in time. Accordingly, the stability analysis is performed using Bolotin's method and Floquet theory. Stability maps for varying velocity of the vehicle, frequency and amplitude of the force oscillations are obtained. Periodically placed circumferential stiffeners are proposed as means to enhance the stability of the considered class of shells. The presented results indicate how the stiffening rings significantly extend the range of stable operating conditions by reducing the regions of dynamic instability, and suggest that optimal stiffened designs may be identified to achieve stability at given operating speeds and under periodic longitudinal forces.

Keywords: Supercavitating vehicles; Stiffened shells; Dynamic buckling stability

1. Introduction

Underwater vehicles such as torpedoes and submarines are limited in maximum speed by the considerable drag produced by the flow friction on the hull skin. Speeds of 40 m/s are usually considered as a maximum limit, and most practical systems are limited to less than half this value. While low speed is advantageous for acoustic and hydrodynamic efficiency, the achievement of high speed for underwater vehicles and projectiles cannot be obtained using conventional hydrodynamics. When a body moves through water at sufficient speed, the fluid pressure drops locally below the level that sustains the liquid phase, and a low-density gaseous cavity forms. Flows exhibiting cavities entirely enveloping the moving body are called "supercavitating". In supercavitating flows, the liquid phase does not contact the moving

* Tel.: +1-404-894-3078; fax: +1-404-894-2760.
E-mail address: massimo.ruzzene@ae.gatech.edu (M. Ruzzene).

0020-7683/$ - see front matter © 2003 Published by Elsevier Ltd.
doi:10.1016/j.ijsolstr.2003.10.008

body over most of its length, thus making the skin drag almost negligible. Several new and projected supercavitating underwater vehicles exploit supercavitation as a means to achieve extremely high submerged speeds and low drag (Miller, 1995). The size of existing or notional supercavitating high-speed bodies ranges from that of projectiles to heavyweight full-scale torpedoes (Ashley, 2001; Harkins, 2001). Although extensive efforts have been devoted in the past to the analysis of the fluid dynamic characteristics of supercavitating vehicles (Harkins, 2001; Savchenko, 2001), very little research has been dedicated so far to the evaluation of the structural behavior of slender elastic bodies traveling underwater at high speed in supercavitating regimes. Much of the previous and current studies on guidance, control and stability have considered supercavitating vehicles as rigid bodies (Rand et al., 1997; Kirschner et al., 2002; Vasin, 2001), or mostly have addressed the hydrodynamic characteristics of the water/cavity system (Savchenko, 2001; Vasin, 2001).

In supercavitating underwater vehicles, the interaction between the water and the cavitator nose is particularly important as the drag force increases approximately with the square of the vehicle's speed and thus can become very high (Vasin, 2001). The drag force compresses axially the body and may cause its buckling. Buckling clearly corresponds to structural failure and therefore has been identified as one of the limiting factors for the operating speed of supercavitating vehicles (Vasin, 2001). Buckling stability is a major concern for the structural safety of supercavitating projectiles, which reach velocities of the order of 1500 m/s (Harkins, 2001). For cylindrical structures such as torpedoes, the value of the critical buckling velocity may approach the limits currently pursued for supercavitating vehicles (Ashley, 2001). Buckling stability hence needs to be addressed in order to assess the structural safety limits of supercavitating torpedoes and should be considered in an effort to extend their operating range. In addition, the transient, unsteady nature of the cavitation process and the resulting time-dependent properties of the cavity and of its interactions with the vehicle require investigating the structural behavior of supercavitating vehicles when acted upon time-varying forces. In particular, variations in the velocity of forward motion, oscillations and shape variations of the cavity, and the complex interaction of the propeller forces with the cavity re-entrant jet cause the drag and the propeller force sustaining the vehicle's motion to be time-dependent (Kirschner et al., 2001; Kirschner and Imas, 2002; Semenenko, 2001a,b; Stinebring et al., 2001). The determination and the analysis of these interactions and the characterization of their dynamic effect are essential in defining the structural stability of supercavitating vehicles.

The goal of this paper is to investigate the dynamic buckling characteristics of supercavitating bodies, modeled as elastic axisymmetric shells. The shells are acted upon by a system of axial forces which are considered to vary periodically in time and are defined in terms of the speed of the vehicle, and period and amplitude of the oscillations. The influence of these parameters on the shell's dynamic stability is assessed through a finite element (FE) model, formulated to predict mass and stiffness properties of the considered class of shells. The FE formulation is used to express the equation of motion of the shell as a Mathieu/Hill equation, whose stability can be studied using Floquet theory and/or Bolotin's method (Bolotin, 1964). The developed FE model also accounts for the effect of circumferential stiffening rings equally spaced along the shell length, which are here applied and used as means for enhancing the shells' stability. Periodically placed stiffening rings have been already proposed to reduce vibrations in supercavitating vehicles resulting from their periodic impacts with the cavity water/interface (tail-slaps) (Ruzzene and Soranna, 2002). The study presented in (Ruzzene and Soranna, 2002) were based on previous results on the dynamic response of periodically stiffened shells (see for example Akl et al., 2002). The effectiveness of periodically located stiffeners in enhancing the dynamic buckling stability of supercavitating bodies is here evaluated by considering different configurations and geometry for the rings. The encouraging performance for the considered configurations suggests that the location and the dimensions of the rings should be optimized in order to achieve stability with minimum added weight. Furthermore, the results presented here and in (Ruzzene and Soranna, 2002) indicate that the stiffening rings may be designed and optimized in order to simultaneously achieve vibration reduction and enhanced buckling stability. The paper is organized in five

sections. In the first section a brief introduction is given. Section 2 outlines the formulation for the axisymmetric shell model and presents the resulting equation of motion. Section 3 describes the considered buckling forces and summarizes the principles of Floquet theory and Bolotin's method for the analysis of the shell's stability. Section 4 presents numerical results obtained for various combinations of the buckling forces and different shell configurations, while Section 5 summarizes the main results of the work and gives recommendations for future research.

2. Finite element formulation

2.1. Overview

The FE model is formulated using the coordinate system and the degrees of freedom shown in Fig. 1. The geometry of the structure is used to reduce the dimensions of the problem through a semi-analytical procedure whereby variables are expanded as Fourier series in the circumferential angle θ. The orthogonality property of harmonic functions decouples the contributions of the components of the series and allows a separate analysis for each circumferential harmonic (Leissa, 1973; Zienkiewicz, 1971; Cook et al., 2002).

2.2. Strain–displacement relationships

The thin-shell approximation is here considered, so that through the thickness normal and shear strains can be neglected (Leissa, 1973). The total strain state in the shell is expressed as a combination of linear and non-linear components:

$$\underline{\varepsilon} = \underline{\varepsilon}^{(\mathrm{l})} + \underline{\varepsilon}^{(\mathrm{nl})} \tag{1}$$

where $\underline{\epsilon} = \{\, \varepsilon_x \quad \varepsilon_\theta \quad \gamma_{x\theta} \,\}^{\mathrm{T}}$ is the vector describing the strain state in the shell.

The linear strains $\underline{\varepsilon}^{(\mathrm{l})}$ are related to the mid-surface displacement through Flugge shell equations (Leissa, 1973; Flugge, 1973; Yamaki, 1984):

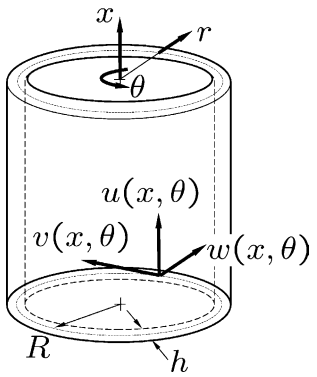

Fig. 1. Degrees of freedom and coordinate system.

$$\begin{aligned}
\varepsilon_x^{(l)} &= u_x - r w_{xx} \\
\varepsilon_\theta^{(l)} &= \frac{v_\theta}{R} + \frac{w}{R+r} - \frac{r}{R}\frac{w_{\theta\theta}}{r+R} \\
\gamma_{x\theta}^{(l)} &= \frac{u_\theta}{R+r} + \frac{R+r}{R} v_x - w_{x\theta}\left(\frac{r}{R} + \frac{r}{R+r}\right)
\end{aligned} \tag{2}$$

where the subscripts 'x' and 'θ' denote partial differentiation, $u = u(x,\theta)$, $v = v(x,\theta)$, $w = w(x,\theta)$ are the axial, tangential and radial displacement of the shell's mid-surface, and R is the mid-surface radius (Fig. 1). The non-linear strain components are expressed as (Yamaki, 1984):

$$\begin{aligned}
\varepsilon_x^{(nl)} &= \frac{1}{2}[u_x^2 + v_x^2 + w_x^2] \\
\varepsilon_\theta^{(nl)} &= \frac{1}{2R^2}[u_\theta^2 + (v - w_\theta)^2 + (w + v_\theta)^2] \\
\gamma_{x\theta}^{(nl)} &= \frac{1}{R}[u_x u_\theta + v_x(w + v_\theta) - w_x(v - w_\theta)]
\end{aligned} \tag{3}$$

2.3. Kinetic and strain energy

The shell strain energy is expressed as:

$$U = U^{(l)} + U^{(nl)} \tag{4}$$

where $U^{(l)}$ and $U^{(nl)}$ are strain energy terms corresponding respectively to the linear and non-linear strains. The strain energy can be written as:

$$U = \frac{1}{2}\int_V \underline{\varepsilon}^{(l)T} \cdot \mathbf{C} \cdot \underline{\varepsilon}^{(l)}\, dV + \frac{1}{2}\int_V \underline{\sigma}_0^T \cdot \underline{\varepsilon}^{(nl)}\, dV \tag{5}$$

where V is the volume of the shell, $\mathbf{C}$ is the stiffness matrix for the shell material, and $\underline{\sigma}_0$ is the stress vector corresponding to the applied buckling loads.

The shell kinetic energy is:

$$T = \frac{1}{2}\int_V \rho(\dot{u}^2 + \dot{v}^2 + \dot{w}^2)\, dV \tag{6}$$

where ρ is the density of the shell's material.

2.4. Degrees of freedom and shape functions

The axisymmetric geometry of the structure allows a semi-analytical formulation for the shell FE model (Zienkiewicz, 1971). The generalized displacement field is expanded by Fourier Series in the circumferential direction according to the following expression:

$$\underline{u}(x,\theta) = \sum_n \mathbf{R}(n,\theta)\underline{u}(n,\theta) \tag{7}$$

with n denoting the nth circumferential harmonic and where:

$$\underline{u} = \{\, u \quad v \quad w \,\}^T \tag{8}$$

and

$$\mathbf{R}(n,\theta) = \begin{bmatrix} \cos n\theta & 0 & 0 \\ 0 & \sin n\theta & 0 \\ 0 & 0 & \cos n\theta \end{bmatrix} \tag{9}$$

The displacement components associated with harmonic n are predicted by discretizing the shell with one-dimensional elements bounded by two nodal points. Each node has 4 degrees of freedom to describe axial, radial and circumferential displacements as well as the rotation about the circumferential axis. The dynamic behavior of each element can be thus described in terms of the following nodal displacement vector:

$$\underline{\delta}_n^{(e)} = \{\, u_{n_i} \quad v_{n_i} \quad w_{n_i} \quad w_{xn_i} \quad u_{n_f} \quad v_{n_f} \quad w_{n_f} \quad w_{xn_f} \,\}^T \tag{10}$$

where i and f denote respectively the element initial and final node. The longitudinal and circumferential displacements are assumed to vary linearly along the axial coordinate x, while cubic polynomials interpolate the radial displacement. The following relations thus hold:

$$\underline{u}(n,x) = \mathbf{N}(x)\underline{\delta}_n^{(e)} \tag{11}$$

where $\mathbf{N}(x)$ is the matrix of the shape functions.

The linear strain component associated with the nth harmonic is expressed as:

$$\underline{\varepsilon}^{(l)} = \sum_n \mathbf{R}(n,\theta)\mathbf{B}(n,r,x)\underline{\delta}_n^{(e)} \tag{12}$$

where $\mathbf{B}(n,r,x)$ is an interpolation matrix obtained by substituting Eqs. (11) and (12) into Eqs. (2) and (3). Expressions for the interpolation matrix $\mathbf{B}$ can be found in (Akl et al., 2002).

2.5. Mass, stiffness and geometric matrices

The interpolation of displacements and strains are used to express the element strain and kinetic energy in terms of the nodal displacement vector $\underline{\delta}_n^{(e)}$. After integration along the circumferential direction, the linear strain energy can be written as:

$$U^{(l)} = \frac{1}{2}\sum_n U_n^{(l)} = \frac{1}{2}\sum_n \underline{\delta}_n^{(e)T}\mathbf{K}_n^{(e)}\underline{\delta}_n^{(e)} \tag{13}$$

where $\mathbf{K}_n^{(e)}$ is the element stiffness matrix for the nth harmonic:

$$\mathbf{K}_n^{(e)} = \pi\int_0^{L^{(e)}}\int_{-h/2}^{h/2} \mathbf{B}^T(n,r,x)\cdot\mathbf{C}\cdot\mathbf{B}(n,r,x)R\,dr\,dx \tag{14}$$

In Eq. (14), $L^{(e)}$ and h denote respectively the element's length and radial thickness.

Similarly, the element kinetic energy can be rewritten as:

$$T = \frac{1}{2}\sum_n T_n = \frac{1}{2}\sum_n \dot{\underline{\delta}}_n^{(e)T}\mathbf{M}^{(e)}\dot{\underline{\delta}}_n^{(e)} \tag{15}$$

where $\mathbf{M}^{(e)}$ is the element mass matrix, which is given by:

$$\mathbf{M}^{(e)} = \pi\rho hR\int_0^{L^{(e)}} \mathbf{N}^T(x)\cdot\mathbf{N}(x)\,dx \tag{16}$$

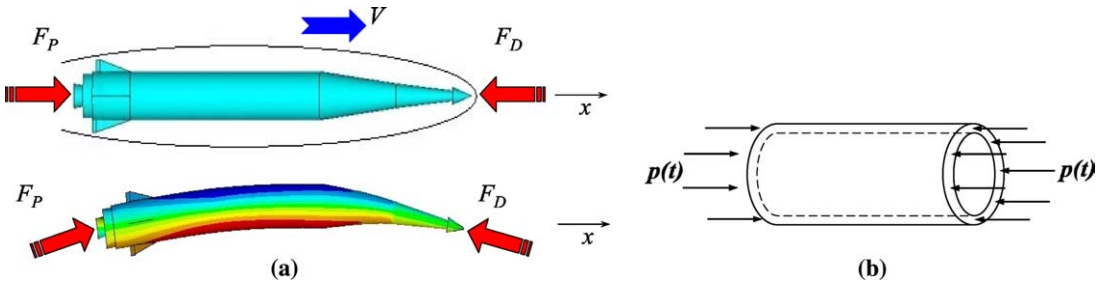

Fig. 2. Buckling of supercavitating vehicles (a) and considered simplified configuration (b).

This study considers axisymmetric axial buckling loads applied according to the configuration shown in Fig. 2. This loading condition is relevant to supercavitating vehicles, as described in the following section (Section 3). Accordingly, the non-linear component of the strain energy can be expressed as:

$$U_n^{(\mathrm{nl})} = \frac{1}{2}\sum_n \int_V \underline{E}_n^{\mathrm{T}} \cdot \mathbf{\Sigma}_0 \cdot \underline{E}_n \,\mathrm{d}V \tag{17}$$

where the vector $\underline{E}_n$ is defined as:

$$\underline{E}_n = \{\, u_x \quad 1/R \cdot u_\vartheta \quad v_x \quad 1/R \cdot v_\vartheta \quad w_x \quad 1/R \cdot (w_\vartheta - v) \,\}_n^{\mathrm{T}} \tag{18}$$

The vector $\underline{E}_n$ is expressed in terms of the nodal degrees of freedom as follows:

$$\underline{E}_n^{(\mathrm{nl})} = \beta(n,r,x)\underline{\delta}_n^{(\mathrm{e})} \tag{19}$$

where β is an interpolation matrix obtained by imposing the shape functions introduced in Eq. (11).

In Eq. (17), matrix $\mathbf{\Sigma}_0$ contains the components of the buckling stress vector $\underline{\sigma}_0 = \{\, \sigma_{0_x} \quad \sigma_{0_\vartheta} \quad \tau_{0_{x\vartheta}} \,\}^{\mathrm{T}}$ and it is given by (Cook et al., 2002):

$$\mathbf{\Sigma}_0 = \mathrm{diag}(\hat{\sigma}_0) \tag{20}$$

with

$$\hat{\sigma}_0 = \begin{bmatrix} \sigma_{0_x} & \tau_{0_{x\vartheta}} \\ \tau_{0_{x\vartheta}} & \sigma_{0_\vartheta} \end{bmatrix} \tag{21}$$

Hence, the element geometric stiffness matrix for axisymmetric buckling loads can be expressed as:

$$\mathbf{Kg}_n^{(\mathrm{e})} = \pi \int_0^{L^{(\mathrm{e})}} \int_{-h/2}^{h/2} \beta(n,r,x)^{\mathrm{T}} \cdot \mathbf{\Sigma}_0^{(\mathrm{e})} \cdot \beta(n,r,x) R \,\mathrm{d}r \,\mathrm{d}x \tag{22}$$

The buckling stresses in each shell element are determined through a separate static axisymmetric ($n = 0$) analysis performed on the considered structure, which gives:

$$\underline{\sigma}_0^{(\mathrm{e})} = \mathbf{C} \cdot \mathbf{B}(0,r,x)\underline{\delta}_0^{(\mathrm{e})} \tag{23}$$

where $\underline{\delta}_0^{(\mathrm{e})}$ is the element nodal displacement vector associated to the $n = 0$ harmonic and corresponding to the applied axisymmetric buckling loads. This formulation for the geometric stiffness matrix is quite general, as it includes the possible effects of loads applied along the axial, radial and circumferential directions. It can be therefore applied to analyze buckling in shells loaded by uniform axial compression, internal or external pressures and/or twisting moments.

The orthogonality properties of the harmonic functions used in the Fourier Series expansion decouple the strain energy of each harmonic component, allow defining a stiffness and geometric matrices for each n, and permit a separate analysis for each harmonic. The displacements and strains resulting from each separate analysis can be recombined through Eqs. (7) and (12) to obtain a complete description of the shell motion and strain state.

2.6. Equation of motion

The shell's equation of motion for a given harmonic n can be obtained by invoking Hamilton's principle, which gives:

$$\mathbf{M}_n\underline{\ddot{\delta}}_n + (\mathbf{K}_n + \mathbf{Kg}_n)\underline{\delta}_n = \underline{0} \tag{24}$$

where $\mathbf{M}_n$, $\mathbf{K}_n$ and $\mathbf{Kg}_n$ are the global FE matrices obtained from the assembly of the element matrices defined in Eqs. (14), (16) and (22), while $\underline{\delta}$ denotes the vector of the global nodal degrees of freedom.

2.7. Validation of finite element formulation

The buckling behavior of plain thin shells under compressive forces is described for example in (Flugge, 1973; Yamaki, 1984; Nagai and Yamaki, 1978). Analytical solutions for shells axially unconstrained and with both ends supported in the tangential and radial directions are given in (Flugge, 1973; Yamaki, 1984). The results from the analytical model are compared with the predictions from a 64 element FE model, formulated according to the procedure described above. Dimensions and material properties considered for the shell are listed in Table 1.

In the FE formulation, the buckling loads are obtained from the solution of the following eigenvalue problem:

$$|\mathbf{K}_n + \mathbf{Kg}_n| = 0 \tag{25}$$

The comparison between the critical loads predicted analytically and through the FE model is presented in Fig. 3, which shows the static buckling loads for values of n varying between 0 and 3. For a given n, each load is identified by the number of half waves along the longitudinal direction, here denoted as m, in the corresponding buckling mode. The plots in Fig. 3 indicate the excellent agreement between the two sets of predictions, thus suggesting the accuracy of the developed FE code.

The results demonstrate the complex characteristics of buckling of cylindrical shells, where, as opposed to beams, critical loads do not increase monotonically with the number of half waves m (Flugge, 1973). This behavior is also responsible for the dynamic stability maps to become quite intricate. For the considered configuration, the curves corresponding to $n = 3$ and $n = 2$ show a minimum for increasing values of m, respectively at $m = 5$ and $m = 2$. In here, the mode $n = m = 2$ is the one occurring for the lowest value of the axial load. The corresponding buckling mode is shown in Fig. 4.

Table 1
Shell material properties and geometry

E (N/m^2)	7.1e10
ρ (kg/m^3)	2700
D (m)	0.2
h (mm)	2.5
L (m)	2.0

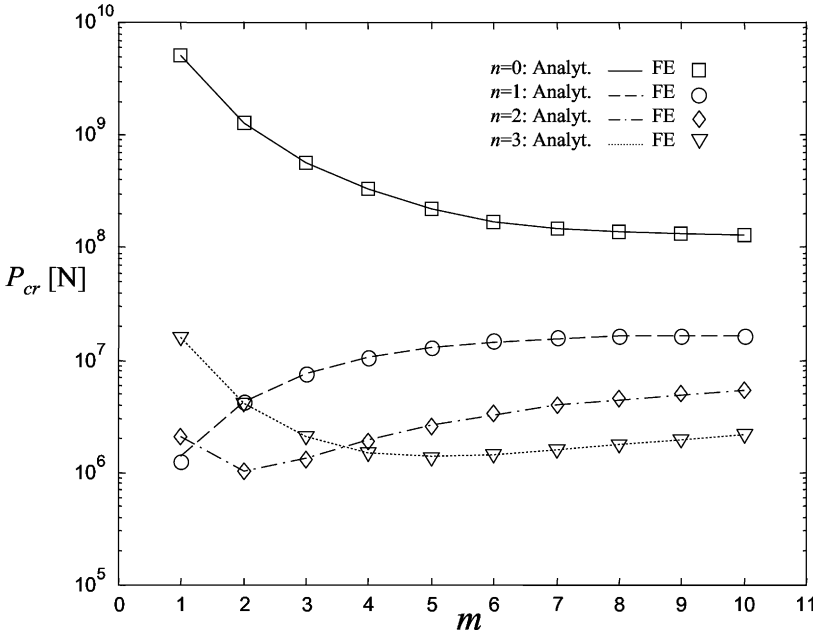

Fig. 3. Static buckling loads: comparison of analytical and FE predictions.

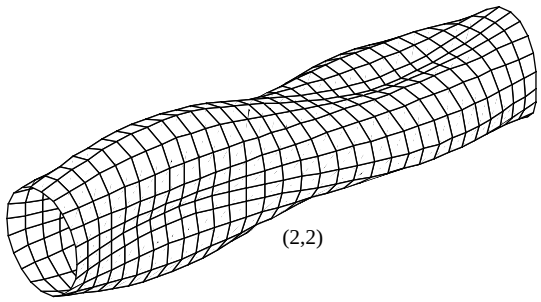

Fig. 4. Buckling mode corresponding to lowest critical load.

3. Buckling forces and techniques for stability analysis

Underwater supercavitating vehicles can be as a first approximation considered as slender elastic bodies, and their structural behavior can be modeled using the shell formulation presented in the previous section. The nature of the forces acting on supercavitating vehicles is very complex and still under extensive experimental and numerical investigations. The results presented herein are intended to provide design guidelines which will help estimating the stability limits for the considered class of vehicles. In addition, the results can be also valuable for the design of other structures whose behavior can be described by a cylindrical shell approximation.

3.1. Overview: buckling forces in supercavitating vehicles

According to the configuration depicted in Fig. 2(a), the vehicle interacts with the liquid phase through its front surface (nose or cavitator), past which the cavity is formed. The drag force experienced by the vehicle during its forward motion is given by (Vasin, 2001; Kirschner et al., 2001):

$$F_{\mathrm{D}} = \frac{1}{2}\rho_{\mathrm{w}} A_{\mathrm{c}} C_{\mathrm{D}}(\sigma, 0) V^2 \tag{26}$$

where ρ_{w} is the density of the fluid (water), A_{c} is the cross section area of the cavitator, and V is the velocity of forward motion of the body. Also in Eq. (26), $C_{\mathrm{D}}(\sigma, 0)$ is the cavitator drag coefficient at zero angle of attack, as defined in (Kirschner et al., 2002; Semenenko, 2001b) and σ is the cavitation number, which is given by:

$$\sigma = \frac{p_\infty - p_{\mathrm{c}}}{1/2\rho_{\mathrm{w}} V^2} \tag{27}$$

where p_∞, p_{c} denote respectively the ambient and cavity pressures. The supercavitation flow regimes, whereby the vehicle's body is completely enveloped by a gaseous cavity, corresponds to small cavitation numbers ($\sigma < 0.1$). Such values can be achieved naturally for velocities of forward motion $V > 50$ m/s. In such conditions, the cavity pressure p_{c} decreases to oscillate about a value close to the saturated water vapor pressure $p_{\mathrm{v}} = 2350$ Pa (at 20 °C) (Semenenko, 2001b). Hence, in this condition, the effects of the corresponding external pressure load on the vehicle's body can be easily neglected.

The unsteady nature of supercavitating flows and of the vehicle/cavity interactions require a complete stability analysis for the considered class of vehicles to consider time-varying components for the applied buckling loads. Associated to the natural supercavitating regimes here considered are cavity shape and pressure oscillations which affect the magnitude of the applied axial loads. Primarily, the cavity oscillations affect the drag coefficient which typically shows periodic impulsive-type increments with respect to the steady state value introduced in Eq. (26). A description of this behavior can be found in (Kirschner et al., 2001), where both experimental and numerical results are discussed. Moreover, the motion of supercavitating vehicles is guided and controlled through a set of fins located close to the tail of the vehicle (see Fig. 2). The fins generate lift as well as drag forces which depend upon the vehicle's motion and the hydrodynamic behavior of the cavity. The fins act as cavity-piercing hydrofoils, and experience unsteady drag forces oscillating at frequencies approximately in the kHz range. Experimental evidence of such oscillations can be found in (Stinebring et al., 2001). In addition, the propulsion force F_{P} that sustains the vehicle motion interacts with the cavity re-entrant jet. The nature and the characteristics of these interactions are still under extensive investigations (see for example (Kirschner and Imas, 2002)), but initial studies have highlighted the presence of significant oscillations, which cause the propulsion not to be constant in time. Finally, even during horizontal flight, the vehicle undergoes periodic impacts (tail-slaps) with the cavity wall or is subject to planing forces, which also have time-dependent axial components (Kirschner et al., 2002). The combination of all these effects, in addition with the influence of the vehicle's maneuvers and the associated interactions with the cavity, require the analysis of the vehicle's stability to consider time-varying forces. Since the behavior of axial forces on supercavitating vehicles is still being evaluated and fully characterized, and due to the complexity of the considered system, simplified formulations for the applied axial loads need to considered at this time. Both harmonic-type as well as periodic pulse-type forces are used for the analysis, with fundamental period varying over a range that covers a wide spectrum of operating conditions.

3.2. Considered time-variations for the axial force

The axial force $p(t)$ is represented as the sum of a constant component and of a time varying term, which accounts for the oscillations of the force with respect to its constant, steady flow value. The considered axial force is expressed as:

$$\begin{aligned} p(t) &= p_0 + p_{\mathrm{d}}(t) \\ p(t) &= p_0 + p_{\mathrm{d}0}\Phi(t) \\ p(t) &= p_0(1 + \beta\Phi(t)) \end{aligned} \tag{28}$$

In Eq. (28), p_0 denotes the constant component of the distributed axial force, while $p_{\mathrm{d}0}$ and $\Phi(t)$ respectively define amplitude and variation of the time-varying component. The magnitude $p_{\mathrm{d}0}$ is expressed in terms of p_0 through the ratio $\beta = p_{\mathrm{d}0}/p_0$. The constant component of the total axial force is taken equal to the drag force expressed by Eq. (26), so that the total force per unit area p_0 is given by:

$$p_0 = \frac{F_{\mathrm{D}}}{2\pi Rh} = \frac{\rho_{\mathrm{w}} A_{\mathrm{c}} C_{\mathrm{D}}}{4\pi Rh} V^2 \tag{29}$$

Eq. (29) relates the axial load to the velocity of forward motion of the vehicle V. The following expressions for $\Phi(t)$ are considered:

$$\Phi(t) = \cos \Omega t \tag{30}$$

and

$$\Phi(t) = \begin{cases} 1 & 0 < t < \tau \\ 0 & \tau < t < T \end{cases} \tag{31}$$

where $\Omega = 2\pi/T$ defines the frequency of the oscillations of the axial force. The considered expressions for $\Phi(t)$ given in Eqs. (30) and (31) in general define a variety of periodic variations for the axial force. In particular, the expression of $\Phi(t)$ given in Eq. (31) describes a force characterized by a sequence of rectangular pulses of duration τ, which approximately reproduces measured oscillations and variations of the drag coefficient at the nose (Stinebring et al., 2001). The performed dynamic buckling analysis evaluates the effects on stability of frequency Ω, force ratio β and pulse duration τ.

The equation of motion for the shell (Eq. (24)) can be conveniently rewritten as:

$$\mathbf{M}_n \ddot{\underline{\delta}}_n + (\mathbf{K}_n + (1 + \beta\Phi(t)) \cdot \mathbf{Kg}_n)\underline{\delta}_n = \underline{0} \tag{32}$$

Eq. (32) is a system of N 2nd order ordinary differential equations, N being the number of degrees of freedom used to discretize the shell structure. Eq. (32) has periodic coefficients as a result of the time-varying axial force and can be characterized as a Mathieu/Hill equation (Bolotin, 1964). The FE formulation in Eq. (32) is a general framework within which generally varying thickness profiles for the shell, as well as the presence of circumferential stiffening rings can be easily accounted for.

Separate analyses are performed for each harmonic n to evaluate the conditions of instability for each circumferential mode order, and to identify the order n where instability occurs for the lowest load values. The evaluation of the buckling behavior for various values of n identifies limit operating conditions for the considered class of supercavitating vehicles, and potentially predicts their failure modes.

3.3. Stability analysis using Bolotin's method

The regions of instability for various combinations of the axial force parameters (vehicle's speed V, frequency Ω, and ratio β) can be obtained by applying the method presented in (Bolotin, 1964). The force variation defined in Eq. (28) describes a case of parametric excitation, which causes instability for particular

relationships between the load frequency Ω and the structure's natural frequencies, and for load amplitudes which are significantly lower than those corresponding to static buckling. For sufficiently small load amplitudes, parametric resonance is achieved for frequencies $\Omega = 2\omega_{m,n}/k$, where k is an integer ($k = 1, 2, \ldots$) and where $\omega_{m,n}$ is the mth natural frequency at harmonic n. The parametric excitation conditions defined by $k = 1$, i.e. with $\Omega = 2\omega_{m,n}$, are denoted as *principal parametric resonances*. According to Bolotin's method, a first approximation for the boundaries of the stability regions corresponding to the principal parametric resonances are obtained by imposing in Eq. (32) periodic solutions of the kind:

$$\underline{\delta}(t) = \underline{A}\sin\frac{\Omega t}{2} + \underline{B}\cos\frac{\Omega t}{2} \tag{33}$$

where $\underline{A}$, $\underline{B}$ are arbitrary vectors. Substituting Eq. (33) in Eq. (32) and equating the coefficients of $\sin(\frac{\Omega t}{2})$, $\cos(\frac{\Omega t}{2})$, yields a set of linear algebraic equation in terms of $\underline{A}$, $\underline{B}$. The condition for non-trivial solutions, i.e. for an unstable response of the system, is given by:

$$\left|\mathbf{K}_n + \left(1 \pm \frac{1}{2}\beta\right) \cdot \mathbf{Kg}_n - \frac{\Omega^2}{4}\mathbf{M}_n\right| = \underline{0} \tag{34}$$

where the geometric matrix $\mathbf{Kg}_n$ is calculated for assigned p_0. Imposing β and solving Eq. (34) yields the values of frequency Ω defining the boundaries between stable and unstable conditions. The solutions of the eigenvalue problem in Eq. (34) obtained with the '–' and '+' sign define respectively the upper and lower boundaries of the stability regions.

Imposing periodic solutions with $\Omega = 2\omega_{m,n}/k$ ($k \neq 1$) gives the stability boundaries corresponding to other parametric resonance conditions. The formulation of the method for a generic value of k becomes however quite cumbersome and computationally intensive.

3.4. Stability analysis using Floquet theory

In order to apply Floquet's theory for stability analysis, Eq. (34) is recast in state space form:

$$\dot{\underline{X}}(t) = \mathbf{A}(t)\underline{X}(t) \tag{35}$$

where $\underline{X}(t) = \{\, \dot{\underline{\delta}}(t) \quad \underline{\delta}(t) \,\}^{\mathrm{T}}$ is the column vector of system states, and $\mathbf{A}(t) = \mathbf{A}(t+T)$ is a $2N \times 2N$ periodic matrix. According to Floquet theory, the stability of linear systems defined by ODEs with periodic coefficients can be assessed by evaluating the spectral radius of the system's transition matrix Θ. The transition matrix Θ relates all the states of the system at a given instant of time t, to the states at time $t + T$:

$$\underline{X}(t+T) = \Theta\underline{X}(t) \tag{36}$$

The spectral radius is defined as the absolute value of the highest eigenvalue of the transition matrix. The response of the system described by Eq. (35) is stable if the spectral radius of the transition matrix is equal to or lower than unity. The transition matrix for a system with generally varying periodic coefficients can be obtained through the numerical evaluation of the response after one period T for the following set of initial conditions:

$$\mathbf{Y}(0) = \mathbf{I} \tag{37}$$

where $\mathbf{I}$ is the $2N \times 2N$ identity matrix and $\mathbf{Y}(t)$ is a $2N \times 2N$ matrix containing the states of the system at time t for the considered sets of initial conditions. Eq. (36) can be hence rewritten as:

$$\mathbf{Y}(T) = \Theta(T)\mathbf{Y}(0) = \Theta(T) \tag{38}$$

This approach applies to systems with generally varying coefficients and therefore is very general. The assessment of the stability for a given combination of the system parameters (in this case frequency Ω,

amplitude p_0, and ratio β) requires $2N$ numerical integrations of the system's equation of motion (Eq. (35)). This often makes the evaluation of the stability regions through the application of Floquet's theory a numerically intensive task.

3.4.1. Evaluation of the transition matrix for a step-wise constant axial force

The transition matrix required for the stability analysis according to Floquet's theory can be efficiently evaluated for the axial force described by Eq. (31), which yields a step-wise constant system matrix $\mathbf{A}(t)$ in Eq. (35). The response of the system at time τ and T and can be found as:

$$\begin{aligned} \underline{X}(\tau) &= \mathrm{e}^{\mathbf{A}_1\tau}\underline{X}(0) \quad 0 < t < \tau \\ \underline{X}(T) &= \mathrm{e}^{\mathbf{A}_2(T-\tau)}\underline{X}(\tau) \quad \tau < t < T \end{aligned} \tag{39}$$

Imposing continuity of the states at time $t = \tau$ gives:

$$\underline{X}(T) = \mathrm{e}^{\mathbf{A}_2(T-\tau)}\mathrm{e}^{\mathbf{A}_1\tau}\underline{X}(0) = \Theta(T)\underline{X}(0) \tag{40}$$

where

$$\Theta(T) = \mathrm{e}^{\mathbf{A}_2(T-\tau)}\mathrm{e}^{\mathbf{A}_1\tau} \tag{41}$$

is the transition matrix of the system. For the step-wise time-varying longitudinal force, the evaluation of the transition matrix using Eq. (41) represents a simple alternative to numerical integration. For general periodic variations of the axial forces other numerical techniques can be applied and are currently being tested (Bauchau and Nikishkov, 2001; Hirsch and Smale, 1974).

4. Numerical results

4.1. Configuration for the stiffened shells

The dynamic stability of stiffened axisymmetric cylindrical shells is here investigated. The considered stiffeners are circumferential and equally spaced along the shell length. They are modeled as shell elements of higher thickness, according to the formulation described in Section 2. This simple representation for the stiffeners allows a first assessment of their effectiveness in stabilizing the shell buckling behavior. The buckling forces described in Section 3 are considered in order to perform a comprehensive evaluation of

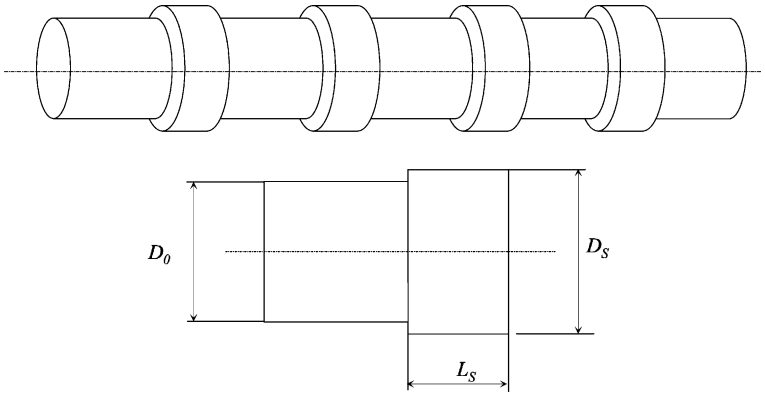

Fig. 5. Schematic of considered stiffened configurations and main dimensions of the stiffeners.

Table 2
Stiffened configurations: number of rings and spacing

Number of rings	Spacing (m)
0 (Plain)	–
8	0.02
16	0.01

Table 3
First natural frequency versus harmonic n

n	Frequency (Hz)
0	8662
1	137
2	353
3	482

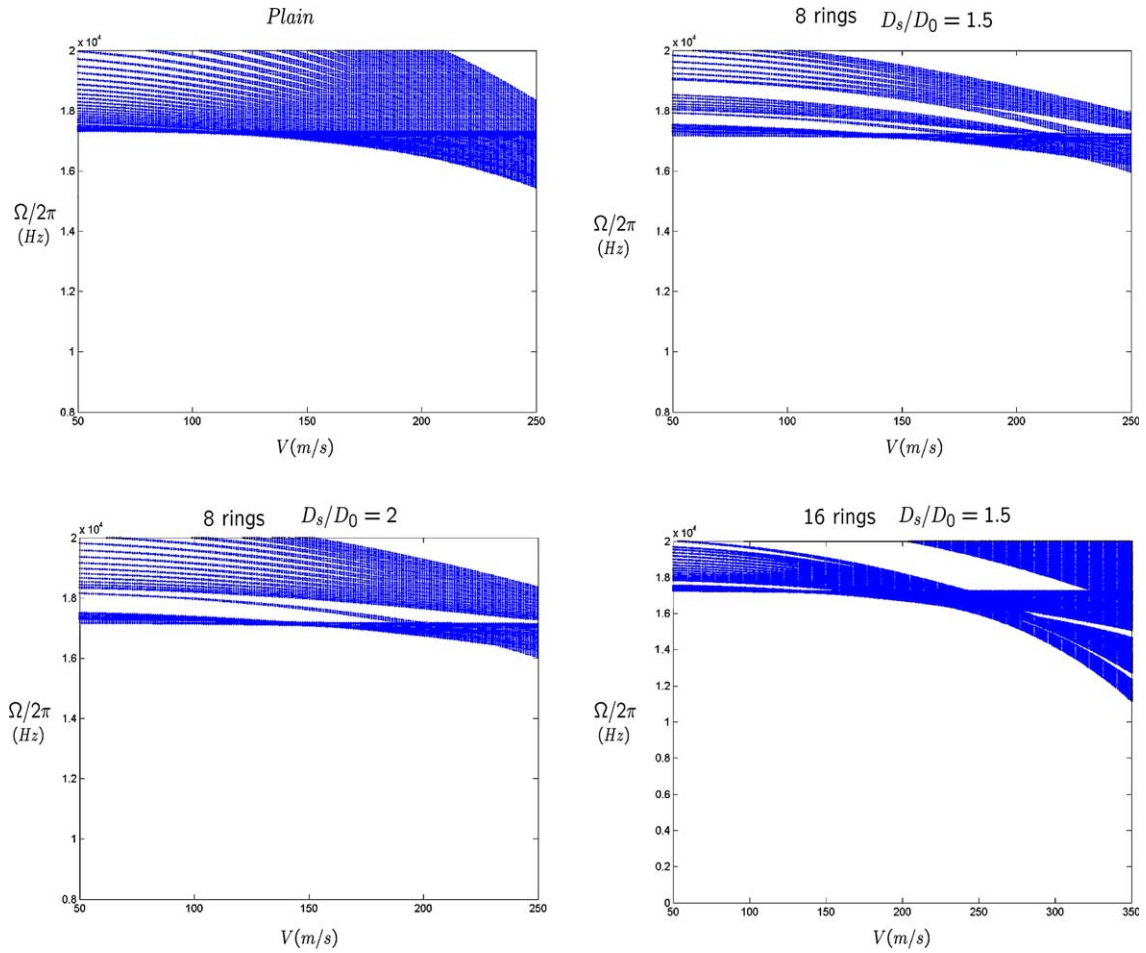

Fig. 6. Principal instability regions for plain and stiffened shells ($n = 0$).

stability when the shell is acted upon by a variety of periodically time-varying longitudinal forces. The analysis can be performed for varying periods of the force ($T = 2\pi/\Omega$), increasing amplitude of the static component p_0, various ratios β and pulse durations τ. For each combination of these parameters, the buckling characteristics of plain shells are compared to the those of stiffened shells of various configurations. The dimensions and the material properties of the plain shell are those listed in Table 1. The stiffening rings have an axial length $L_s = 5$ cm, which is kept fixed throughout the analysis. The considered rings' thickness varies between 0 (i.e. unstiffened, or plain configuration) and 0.005 m, corresponding to $D_s = 2D_0$. The schematic representation of a stiffened shell is shown in Fig. 5, while Table 2 summarizes the considered stiffened configurations.

4.2. Dynamic stability for harmonic axial force

The dynamic stability of plain and stiffened shells is first evaluated for an axial force described by Eq. (30). The results presented in this section are limited to the principal parametric resonance, as predicted using Bolotin's method. For each harmonic order n, the analysis is carried out in a frequency range

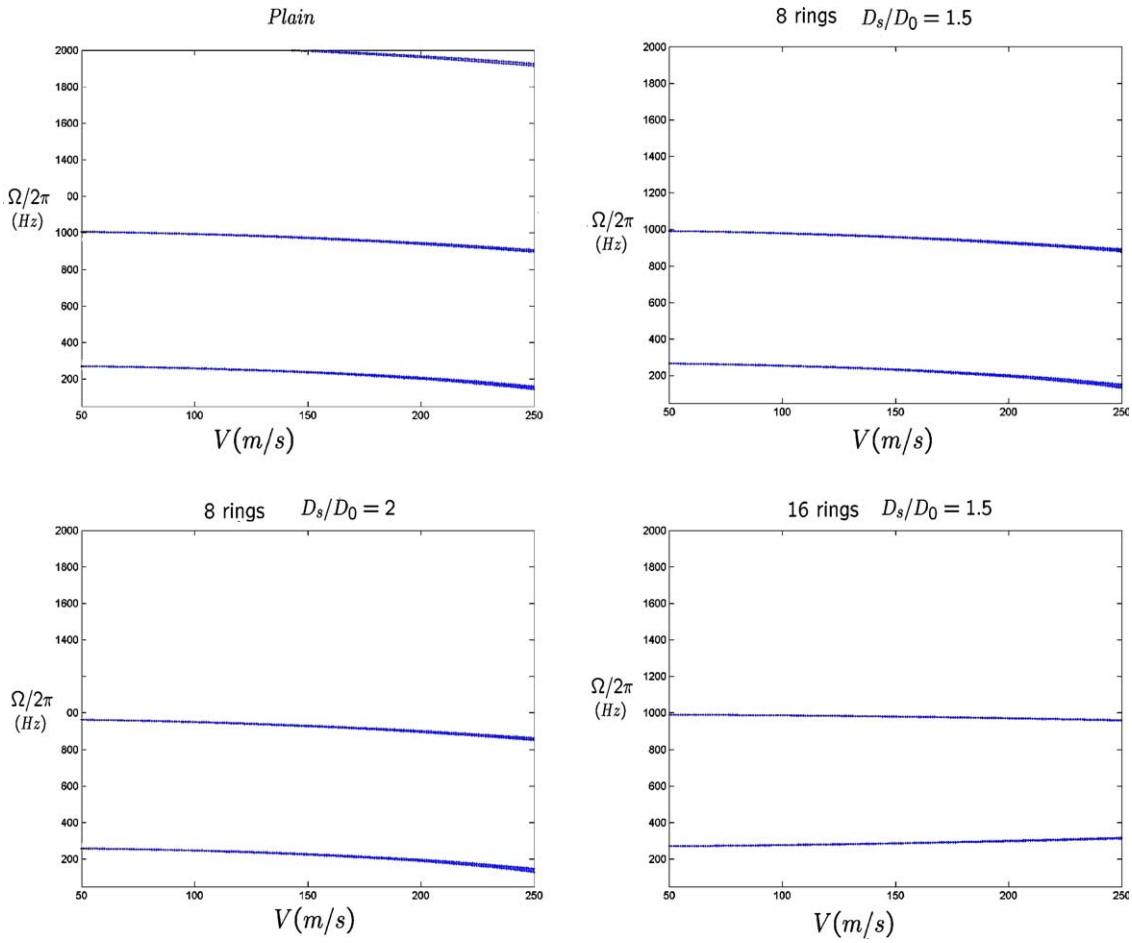

Fig. 7. Principal instability regions for plain and stiffened shells ($n = 1$).

approximately centered at twice the frequency of the lowest radial mode (see Table 3). Results for $\beta = 0.1$ are shown in Figs. 6–9, where the instability regions are represented by dark regions. The maximum value of velocity (250 m/s) considered for the analysis is higher than the operating conditions currently envisioned for supercavitating torpedoes ($\simeq$100 m/s, (Ashley, 2001)), but may represent a limit for future refinements of this concept.

Fig. 6 presents the stability characteristics for the axisymmetric mode ($n = 0$). The first unstable region begins approximately at 17 kHz at low speeds. This limit decreases as the vehicle's velocity, i.e. the magnitude of the applied axial load, increases. Adding the rings substantially modifies the extension as well as the location of the unstable regions. In particular, both 8 and 16 rings reduce the extension of the unstable regions in the considered frequency range. Such a reduction can be primarily explained by the stiffening effect of the rings, which cause an increase in the natural frequencies and associated parametric instability conditions. Such a shift is however limited as the stiffening effect of the rings is balanced by the associated added mass. In addition and more importantly, equally spaced rings affect substantially the dynamic buckling stability of the shell by reducing the extension of the unstable regions. Such a reduction produces an extension of the stable regions above the first critical conditions, as evidently shown in the map for the

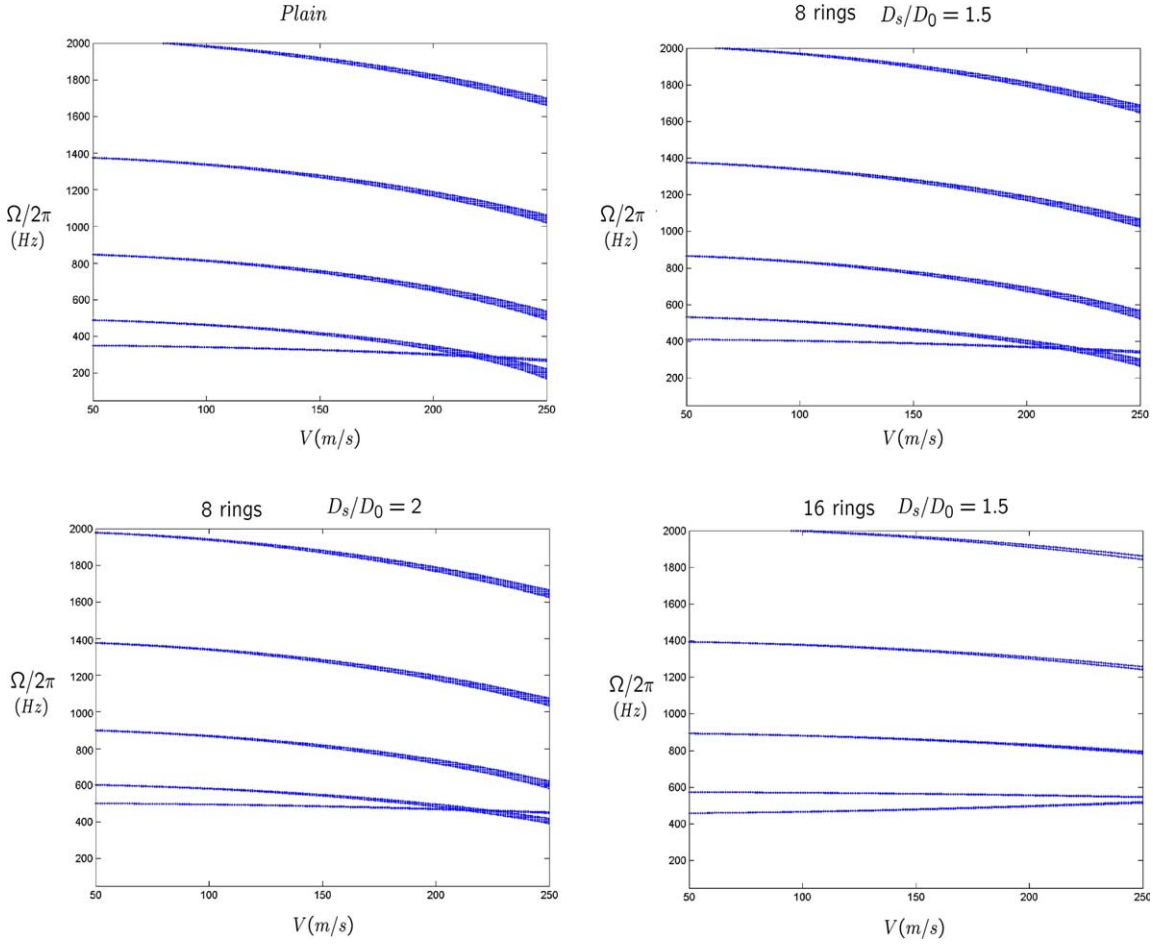

Fig. 8. Principal instability regions for plain and stiffened shells ($n = 2$).

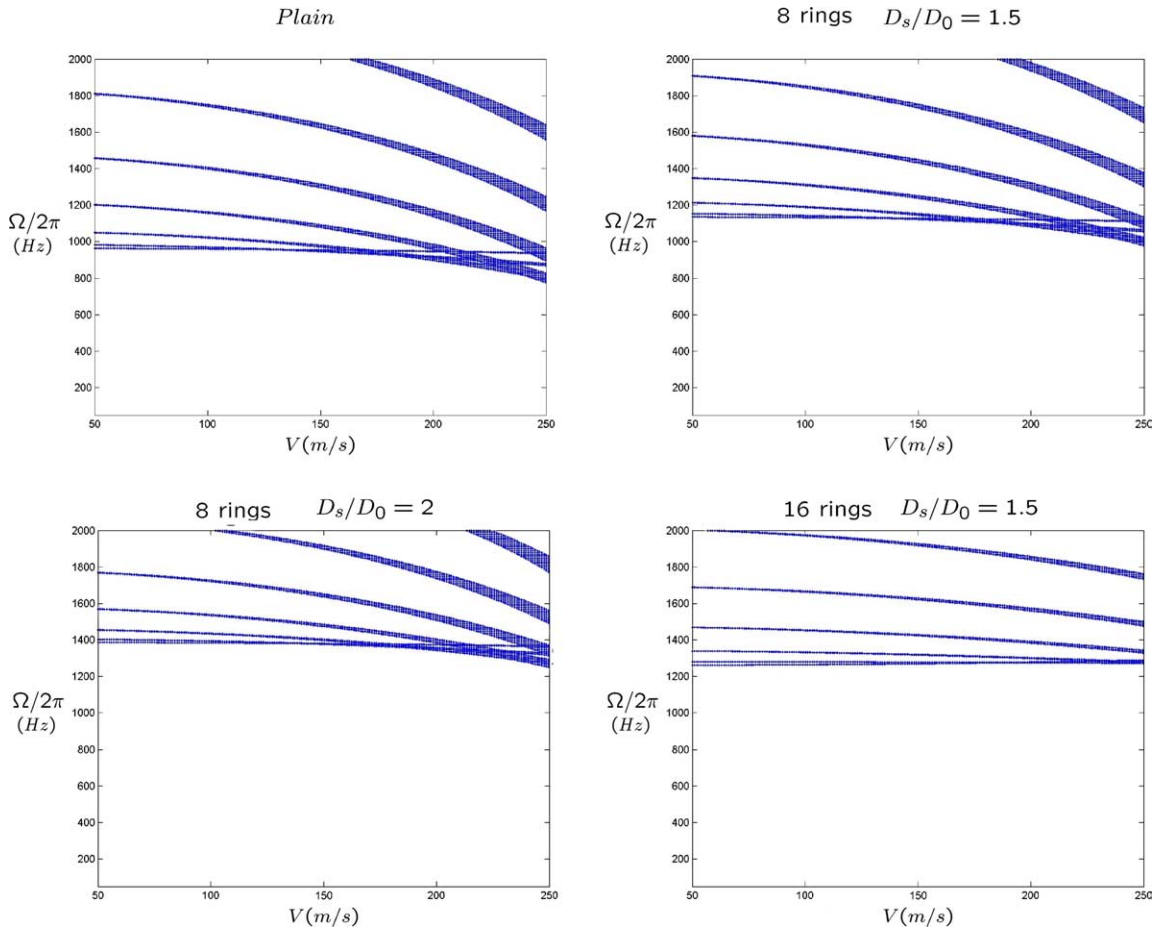

Fig. 9. Principal instability regions for plain and stiffened shells ($n = 3$).

shell with eight rings and $D_s/D_0 = 2$. The extension of these supercritical stable conditions is highly influenced by the number and geometry of the rings, which suggests that the stiffened configurations may need to be optimized in order to achieve stability for assigned values of frequency and velocity. The maps shown in Fig. 7 indicate that instability for $n = 1$ occurs at significantly lower frequencies, as expected from the value of the associated natural frequency (Table 3), and over very narrow regions. The stiffening rings are again effective in enhancing the stability of the vehicle. They eliminate the third unstable region from the considered frequency range, and overall reduce the extension of the two remaining regions. Similar conclusions can be drawn from the analysis of Figs. 8 and 9, which show results respectively for $n = 2$ and $n = 3$.

4.3. Dynamic stability for step-wise periodic axial force

The performance of the considered stiffened configurations is also evaluated when the axial force has a time varying component described by Eq. (31). The stability is evaluated for various combinations of the longitudinal force parameters, which now also include the duration of the rectangular pulse τ. Durations

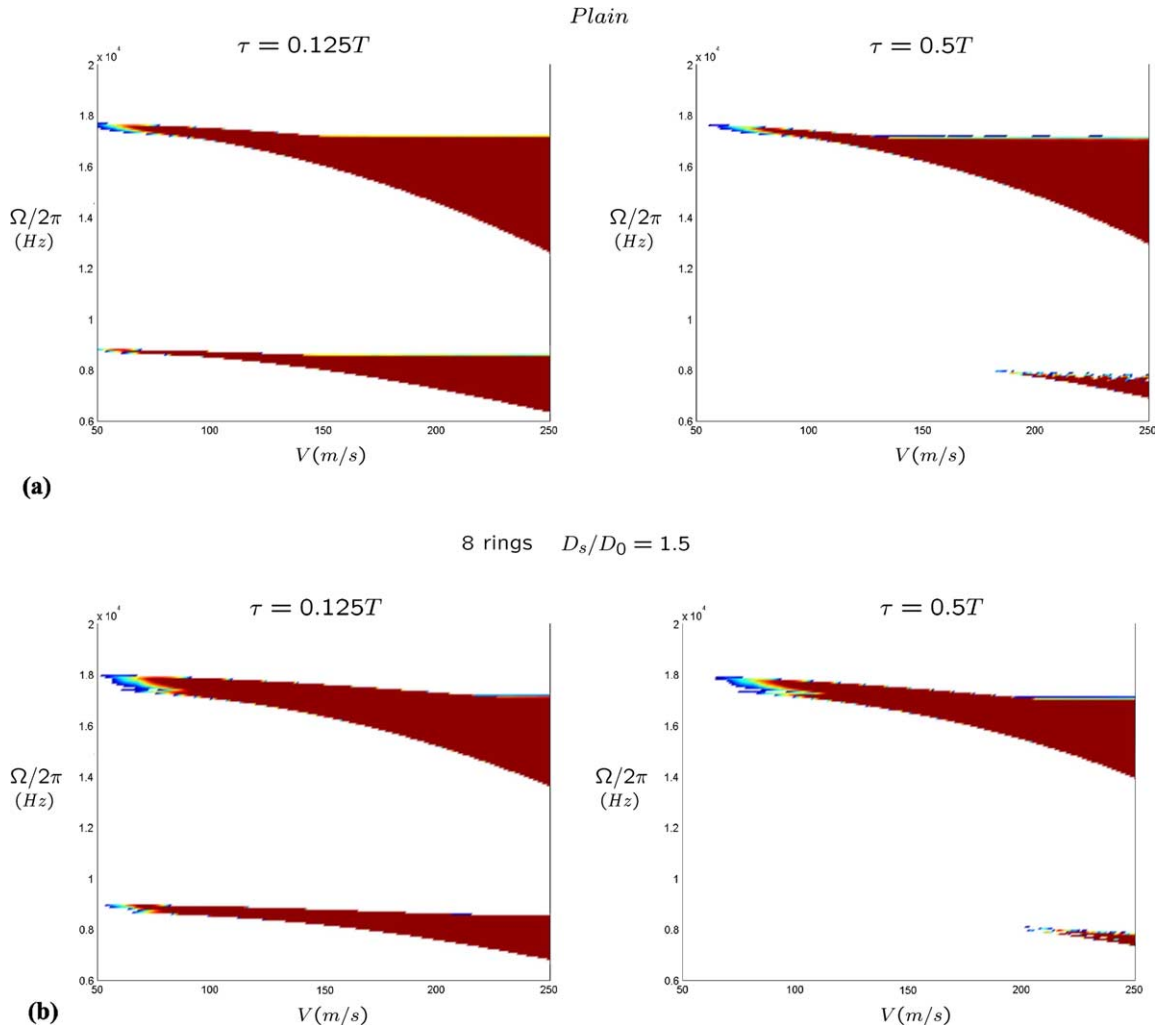

Fig. 10. Unstable regions for periodic axial pulse: plain (a) and stiffened (b) shells ($n = 0$).

$\tau = 0.125T$, and $\tau = 0.5T$, are considered to evaluate the effect of the pulse duration on the extension of the instability regions. Results for plain shells can be found in Figs. 10(a), 11(a), 12(a) and 13(a) which respectively show the stability maps for $n = 0$, 1, 2, and 3. The maps are obtained by plotting the spectral radius of the transition matrix defined in Eq. (41). In order to improve the clarity of the plots, the logarithm of the spectral radius is plotted, so that zero values identify stable combinations of frequency Ω and velocity V. These zero values are estimated within a tolerance of 1e−5 in order to reduce the effects of numerical inaccuracies in the evaluation of the transition matrix. Such tolerance value has been selected after an extensive study aimed at reducing numerical errors, while maintaining the accuracy in the estimation of the stable regions. Finally, a 2-color map was enforced in the plots to identify unstable regions by a single dark color.

The results for $n = 0$ shown in Fig. 10(a) indicate the presence of two major instability regions in the considered frequency range. The additional region, centered at approximately 8600 Hz, corresponds to the

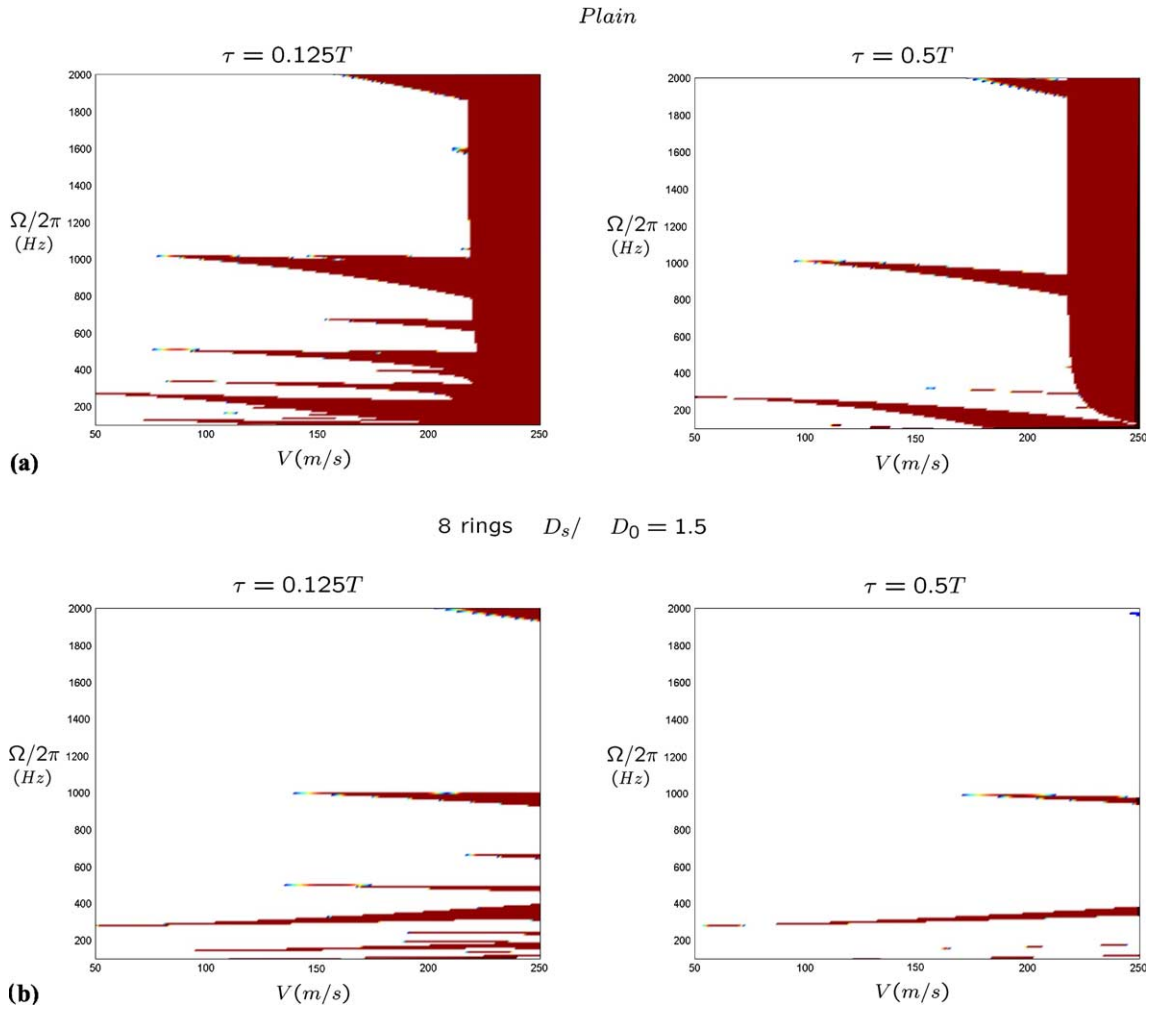

Fig. 11. Unstable regions for periodic axial pulse: plain (a) and stiffened (b) shells ($n = 1$).

second parametric resonant condition, which occurs for frequencies $\Omega = 2\omega_i/k$, ($k \neq 1$). As opposed to Bolotin's method, Floquet theory predicts all instabilities in the considered frequency range, without the capability of discriminating between primary and secondary parametric resonance. The maps of Fig. 10(a) indicate that the duration of the pulse significantly affects secondary parametric resonance conditions, which become more important for shorter pulse durations ($\tau = 0.125T$ in Fig. 10(a)). Similar conclusions can be drawn from the maps corresponding to higher values of n which are shown in Figs. 11(a), 12(a), and 13(a). Particularly for $n = 2$ and $n = 3$, the considered variation for the axial force induces instability in a wide range of conditions. The importance of secondary parametric resonance conditions is evident and again more important for small pulse duration.

The effect of the stiffening rings is shown in Figs. 10(b), 11(b), 12(b), and 13(b). The rings are again effective in increasing the shell's stability for this second considered variation for the axial force. The effectiveness for $n = 0$ modes is limited, as the addition of the rings slightly reduces the extension of the two parametric resonance regions, more remarkably in the case of $\tau = 0.5T$. The influence of the rings is more

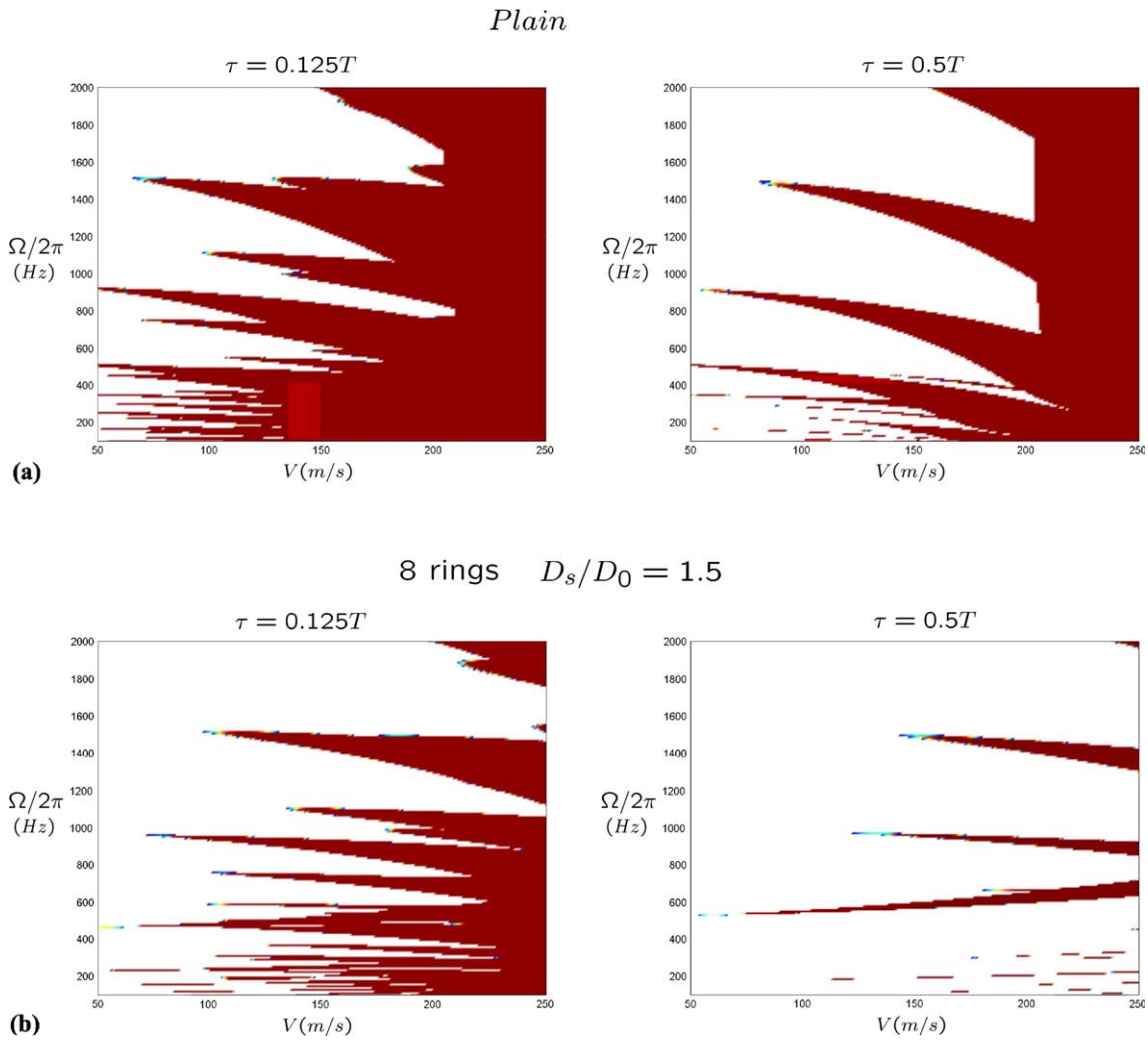

Fig. 12. Unstable regions for periodic axial pulse: plain (a) and stiffened (b) shells ($n = 2$).

dramatic for higher order lobar modes, where significant reductions of the unstable regions can be consistently observed.

5. Conclusions

The dynamic buckling stability of supercavitating underwater vehicle is here analyzed and controlled using periodically placed circumferential stiffening rings. Supercavitating underwater vehicles undergo very high longitudinal forces as a result of their interaction with the water. The magnitude of this force is approximately proportional to the square of the velocity of forward motion of the vehicle and tends to be very high. In addition, the unsteady behavior of the cavity and of the interactions of the vehicle with the cavity/

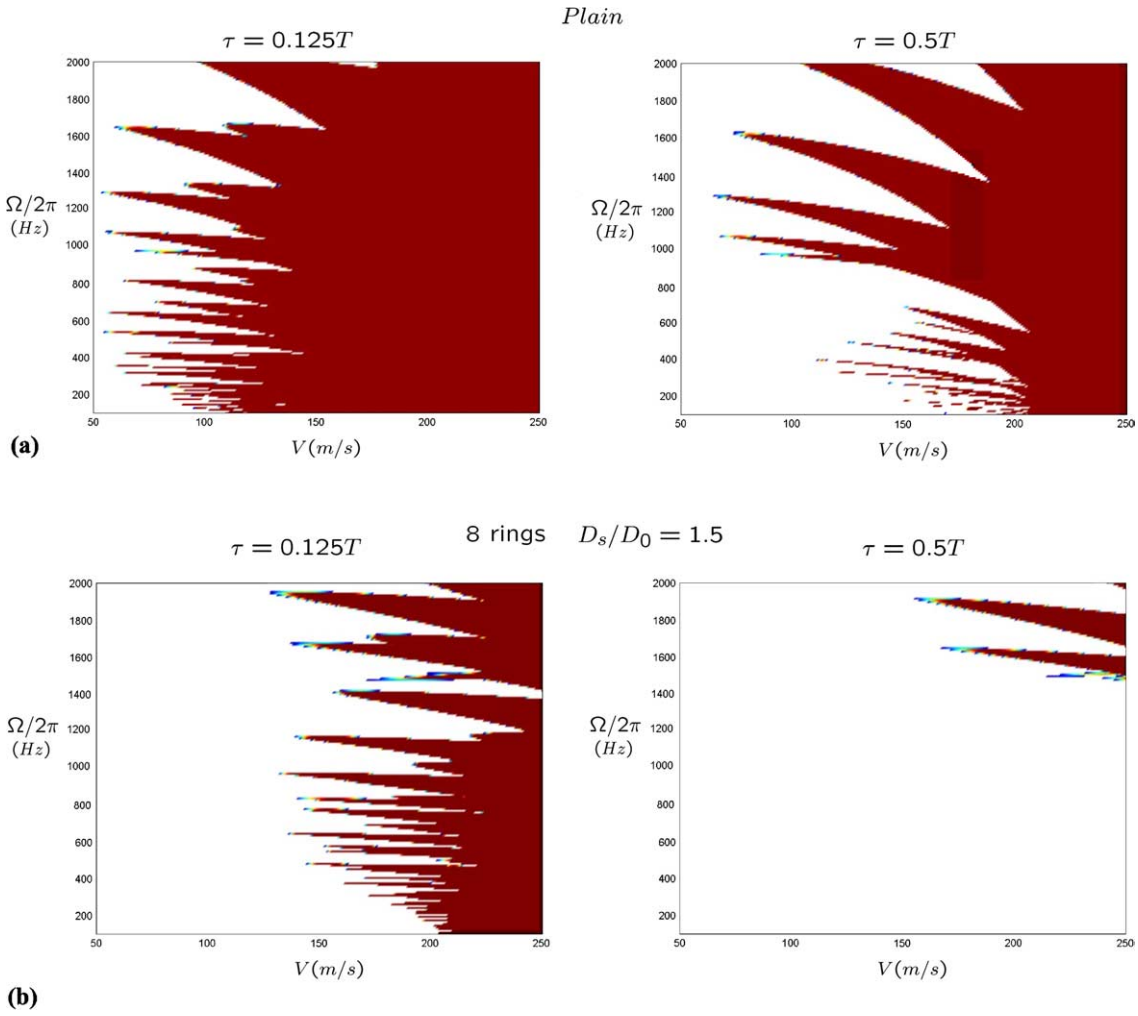

Fig. 13. Unstable regions for periodic axial pulse: plain (a) and stiffened (b) shells ($n = 3$).

water interface requires the stability of supercavitating vehicles to be considered as a case of dynamic buckling. The supercavitating vehicles are modeled as thin axisymmetric shells. A FE model is developed to predict the shells behavior and to perform the buckling analysis. The longitudinal forces are considered to vary periodically in time, thus potentially causing parametric resonance conditions. The longitudinal forces are described as purely harmonic functions as well as step-wise periodic functions. For the case of harmonic forces, the buckling analysis is performed using Bolotin's method, which provides an approximated expression for the stability boundaries related to the principal parametric resonance. The particular nature of the step-wise time variation considered as a second case, allows the evaluation of the system's transition matrix without the need for numerical integration. This makes Floquet theory applicable in this case for a complete evaluation of the extension of the stability regions. For both considered force variations, the extension of the stability regions is evaluated for varying velocity of the vehicle, frequency and amplitude of the force oscillations, and pulse duration. The comparison of the buckling characteristics of plain and stiffened shells of various configurations indicates how the stiffening rings substantially extend the range of

stable operating conditions. The presented results suggest that optimal stiffened designs may be identified to achieve stability at given operating speeds and under specified oscillations of the longitudinal force. Future work will hence attempt to implement an optimization process having the maximization of the extension of the stable regions as one of the objective functions. The effect of non-uniformly distributed axial forces varying periodically or non-periodically in time will be also evaluated.

Acknowledgements

The work is supported through the Young Investigator Program of the Office of Naval Research (Grant # N00014-03-1-0168). The author gratefully acknowledges the guidance and the support of Dr. Kam Ng, Technical Monitor and Program Manager. The author also wishes to thank the reviewers, whose useful comments helped to substantially improve the quality of the paper.

References

Akl, W., Ruzzene, M., Baz, A., 2002. Optimum design of underwater stiffened shells. Structural and Multidisciplinary Optimization (23), 297–310.

Ashley, S., 2001. Warp-drive Underwater. Scientific American.

Bauchau, O., Nikishkov, Y.G., 2001. An implicit Floquet analysis for rotorcraft stability evaluation. Journal of the American Helicopter Society (46), 200–209.

Bolotin, V.V., 1964. The Dynamic Stability of Elastic Systems. Holden-Day, Inc.

Cook, R.D., Malkus, D.S., Plesha, M.E., 2002. Concepts and Applications of the Finite Element Method. John Wiley & Sons.

Flugge, W., 1973. Stresses in Shells. Springer-Verlag, New York.

Harkins, T.K., 2001. Hydroballistics: development, theory and some test results. In: 19th International Symposium on Ballistics, Interlaken, Switzerland, 7–11 May 2001.

Hirsch, M.W., Smale, S., 1974. Differential Equations, Dynamical Systems, and Linear Algebra. Academic Press, NY.

Kirschner, I.N., Imas, L.G., 2002. Plume-supercavity interactions. The International Summer Scientific School "High-Speed Hydrodynamic", Cheboksary, Russia, June 2002.

Kirschner, I.N., Fine, N.E., Uhlman, J.S., Kring, D.C., 2001. Numerical modeling of supercavitating flows. RTO AVT Lecture Series on Supercavitating Flows, Von Karman Institute, Brussels, Belgium, February 2001.

Kirschner, I.N., Kring, D.C., Stokes, A.W., Fine, N.E., Uhlman, J.S., 2002. Control strategies for supercavitating vehicles. Journal of Vibration and Control 8, 219–242.

Leissa, A.W., 1973. Vibration of shells. NASA SP-288, Government Printing Office, Washington DC, 1973.

Miller, D., 1995. Going to war in a bubble. International Defense Review, 61–63, December 1995.

Nagai, K., Yamaki, N., 1978. Dynamic stability of circular cylindrical shells under periodic compressive forces. Journal of Sound and Vibration 58 (3), 425–441.

Rand, R., Pratap, R., Ramani, D., Cipolla, J., Kirschner, I., 1997. Impact dynamics of a supercavitating underwater projectile. In: Proceedings of ASME Design Engineering Technical Conferences (DETC), Sacramento Ca, 14–17 September 1997.

Ruzzene, M., Soranna, F., 2002. Impact dynamics of elastic supercavitating underwater vehicles. In: 9th AIAA/ISSMO Symposium on Multidisciplinary Analysis and Optimization, Atlanta, GA, 4–6 September 2002.

Savchenko, Y.N., 2001. Supercavitation: problems and perspectives. In: Proceedings of the 4th International Symposium on Cavitation, Pasadena, CA, 20–23 June 2001.

Semenenko, V.N., 2001a. Dynamic processes of supercavitation and computer simulation. RTO AVT Lecture Series on Supercavitating Flows, Von Karman Institute, Brussels, Belgium, February 2001.

Semenenko, V.N., 2001b. Artificial supercavitation. physics and calculation. RTO AVT Lecture Series on Supercavitating Flows, Von Karman Institute, Brussels, Belgium, February 2001.

Stinebring, D.R., Billet, M.L., Lindau, J.W., Kunz, R.F., 2001. Developed cavitation-cavity dynamics. RTO AVT Lecture Series on Supercavitating Flows, Von Karman Institute, Brussels, Belgium, February 2001.

Vasin, A.D., 2001. Some problems of Supersonic cavitation flows. In: Proceedings of the 4th International Symposium on Cavitation, Pasadena CA, 20–23 June 2001.

Yamaki, N., 1984. Elastic Stability of Circular Cylindrical Shells. North-Holland, Amsterdam.

Zienkiewicz, O.C., 1971. The Finite Element Method in Engineering Science. McGraw-Hill.